Breaking symmetry in device design for self-driven 2D materials based photodetectors

Qi Wang[1], Changjian Zhou[1*], Yang Chai[2*]

1. South China University of Technology, Guangzhou, China

2. The Hong Kong Polytechnic University, Hong Kong, China

*Corresponding Authors: zhoucj@scut.edu.cn or ychai@polyu.edu.hk

Abstract: The advent of graphene and other two-dimensional (2D) materials offers great potential for optoelectronics applications. Various device structures and novel mechanisms have been proposed to realize photodetectors with unique detecting properties. In this minireview, we focus on the self-driven photodetector that has great potential for low-power or even powerless operation required in the internet of things and wearable electronics. To address the general principle of the self-driven properties, we propose and elaborate the concept of symmetry breaking in 2D materials based self-driven photodetectors. We discuss various mechanisms of breaking symmetry for self-driven photodetectors, including asymmetrical contact engineering, field-induced asymmetry, PN homojunction, and PN heterostructure. Typical device examples based on these mechanisms are reviewed and compared. The performance of current self-driven photodetectors is critically assessed and future directions are discussed towards the target application fields.

Keyword: self-driven photodetector, 2D material, symmetry breaking

TOC: By elaborating the concept of symmetry breaking in 2D materials based photodetector, we give a concise and generalized framework which covers existing photodetectors with self-driven properties.

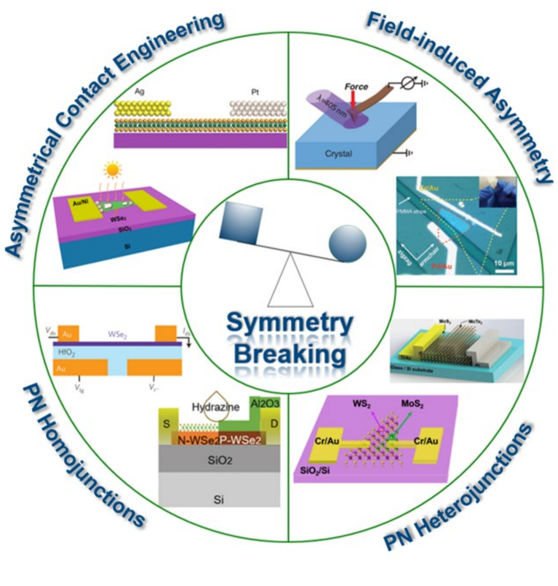

1. Introduction

A photodetector converts light signals into electrical signals, such as current or voltage, based on the photoelectric or photoconductive mechanisms. In recent decades, photodetectors have been widely applied in the cameras embedded in mobile phones and computers[1], astronomical observation[2], remote sensing[3], optical communication[4], and scientific instrument[5]. While silicon-based photodiodes and charge-coupled devices have been adopted in most commercial cameras in our daily life[6], photodetectors based on compound semiconductor, including GaN, InP, and HgCdTe, outperform silicon counterparts in the ultraviolet and infrared range, and novel nanoscale materials have provided rich choices for developing high-performance photodetector for emerging application fields[7, 8].

During the last decade, the advent of two-dimensional (2D) materials offers great potential for optoelectronic applications[8]. Various device structures and novel mechanisms have been proposed to realize photodetectors with unique detecting properties[9]. Currently, the largest market share of photodetectors comes from the mobile phone and personal computer. With the fast development of the Internet of Things (IoT) and the widespread use of wireless sensor networks, an emerging vast market value for photodetectors are expected in the near future[10]. IoT requires low power consumption for the sensor nodes, thus self-sustaining wireless sensors with self-powered or self-driven characteristics are desirable[11]. Moreover, wearable light-weight photodetectors can be widely used in the emerging field of artificial intelligence, which also requires low-power or self-driven photodetectors[12]. The high absorption per atomic thickness, the large range of bandgaps, and the potential integration with silicon data processing platform[13, 14], enable 2D material based photodetector a strong candidate for low-power or even powerless applications in IoT and wearable electronics. It is anticipated that the self-driven 2D material based photodetector could supplement the current silicon and compound semiconductor based photodetectors, which only detect a short range of optical spectrum.

In this minireview, we particularly focus on the photodetectors featuring self-driven properties and discuss the underlying working principles and typical examples of the 2D material based self-driven photodetectors. These device designs are based on a common feature: symmetry breaking. Various 2D materials with unique electronic and optoelectronic properties have provided a great platform to realize the symmetry breaking in 2D based photodetectors. The 2D material self-driven photodetectors in recent studies are mainly based on the metal-semiconductor-metal (MSM) structures, PN junctions, photo-thermoelectric effect, and most recently bulk photovoltaic effect. In section 2, we elaborate the concept of symmetry breaking in each kind of self-driven photodetector and give representative examples. In section 3, we compare different device structures and provide our perspective on future research direction. The review is then concluded with a short summary.

2. Symmetry breaking for self-driven photodetectors

Photodetectors based on Schottky junction require one Ohmic contact which is not easily achievable for 2D materials, so self-driven properties can be obtained by asymmetric contact engineering on the MSM structures, which also applies to the self-driven photodetector based on photo-thermoelectric effect. Field-induced asymmetry, including strain field, strain gradient, and pyroelectric field can be utilized to tune the self-driven properties of photodetectors. The idea of using the photovoltaic effect of a PN junction to design self-driven photodetectors is well known in silicon photodiodes and has recently been extended to build 2D materials based PN junctions. Various methods including thickness engineering, local split gates, chemical doping, and heterostructures formation have been explored towards this purpose.

2.1 Asymmetrical contact engineering

MSM structure that consists of two metal electrodes on the same semiconductor surface detect the incoming light signal by the Schottky junction formed between metal and semiconductor. MSM photodetectors feature a low dark current, a high speed, and ease of integration due to its coplanar structure. As a result, MSM photodetectors have been widely adopted in optical fiber communication, sensing, and guidance[15-17]. However, traditional MSM photodetector built on bulk materials also has the disadvantage of low responsivity, and most importantly, the symmetrical design of the two constituent Schottky junctions results in a zero photocurrent when there is no external voltage bias. To obtain a self-driven MSM photodetector, the symmetry has to be broken to induce a non-zero short-circuit photocurrent (I_{sc}).

As the MSM photodetector can be modeled as two Schottky junctions connected back to back, the I_{sc} under light illumination can be expressed as $I=qG(A_1W_1-A_2W_2)$, where q is the element charge, G is the photo generating rate of charge carriers, and $A_1(A_2)$ and $W_1(W_2)$ are the junction area and depletion width of the first (second) Schottky junction, respectively. Thus, there are two ways to break the symmetry of an MSM photodetector[16, 18-27]. The first way is to utilize the geometrical asymmetrical contact effect, which means the difference in the contact area or contact length between the two constituent Schottky junctions induces a non-zero I_{sc}. In the case of 2D materials, this can be easily demonstrated based on exfoliated irregular flakes or grown triangular flakes. Zhou *et al.* demonstrated a self-driven MSM photodetector based on multilayer WSe_2 flakes[16]. As the Fermi level of WSe_2 is located in the middle of the conduction band minimum (CBM) and valence band maximum (VBM), Ni is chosen as the contact electrodes to obtain a high Schottky barrier for low dark current. As shown in Figure 1a, the MSM photodetector with asymmetrical geometrical contact shows obvious photovoltaic effect. A high responsivity of 2.41 A/W is obtained under zero external bias. Combining the ultralow dark current, a high detectivity of 9.16×10^{11} Jones is achieved. The photovoltaic effect is observed under various laser wavelength illumination ranging from 405 nm to 980 nm. The open-circuit voltage (V_{oc}) increases with increasing contact length difference and reaches 0.42 V when the contact length difference is large enough.

The second way to break the symmetry is to choose contact electrodes with different work functions, which results in a Schottky barrier height difference as well as a different depletion width between the two MS junctions. Early work on using graphene as the channel material and Ti and Pd as the two electrodes showed a fast response speed but a large dark current due to the gapless graphene (Figure 1b)[22]. Gong *et al.* reported an Au-MoS_2-ITO vertical photodetector, in which the Au (5.1eV) and ITO (4.6eV) electrodes exhibit a relatively large difference in work function[20]. The clear photovoltaic effect was observed for the asymmetrical photodetector (Figure 1c). As the multilayer MoS_2 is sandwiched between Au and ITO electrodes (Inset of Figure 1c), a short response time of ~ 64 μs is obtained. By integrating 2D semiconductor material with a traditional bulk semiconductor, Yao *et al.* demonstrated a self-driven Bi-WS_2-Si photodetector featuring a high detectivity of 1.36×10^{13} Jones and a large on/off ratio of 10^6 under zero bias.[24] We note that reported Graphene-TMD-Graphene vertical heterostructures also show a clear photovoltaic effect even the top and bottom electrode materials are the same[23, 25, 26]. However, the observed photovoltaic effect can be still ascribed to the barrier difference between the two MS junctions, because either the graphene preparation method[23] or the bottom-gate electric field induced Fermi level shift[25, 26] will result in the work function difference between the two graphene electrodes. Although the vertical structure exhibits a fast response speed, its responsivity is relatively low and transparent materials should be adopted for the top electrode, which limits the choice of electrode materials. In comparison, a planar structure with In and Au as the two electrodes contacting InSe exhibits a relatively high responsivity of 369 mA/W [19]. While a clear I_{sc} is obtained for these self-driven photodetectors, the V_{oc} is relatively small, at least much smaller than the difference between the work functions of the two electrode materials, which is mainly due to the Fermi level pinning effect. This effect can be mediated by forming van der Waals contacts[28, 29]. Liu et al. demonstrated an Ag-MoS_2-Pt photodetector with van der Waals contacts for both the MS junctions. Figure 1d shows the schematic device structure and the measured *I-V* curves. The responsivity of a monolayer and seven-layer based devices are 7.2 mA/W and 16.6 mA/W, respectively, and a high V_{oc} of 0.76 V is obtained under a 532 nm light illumination[28].

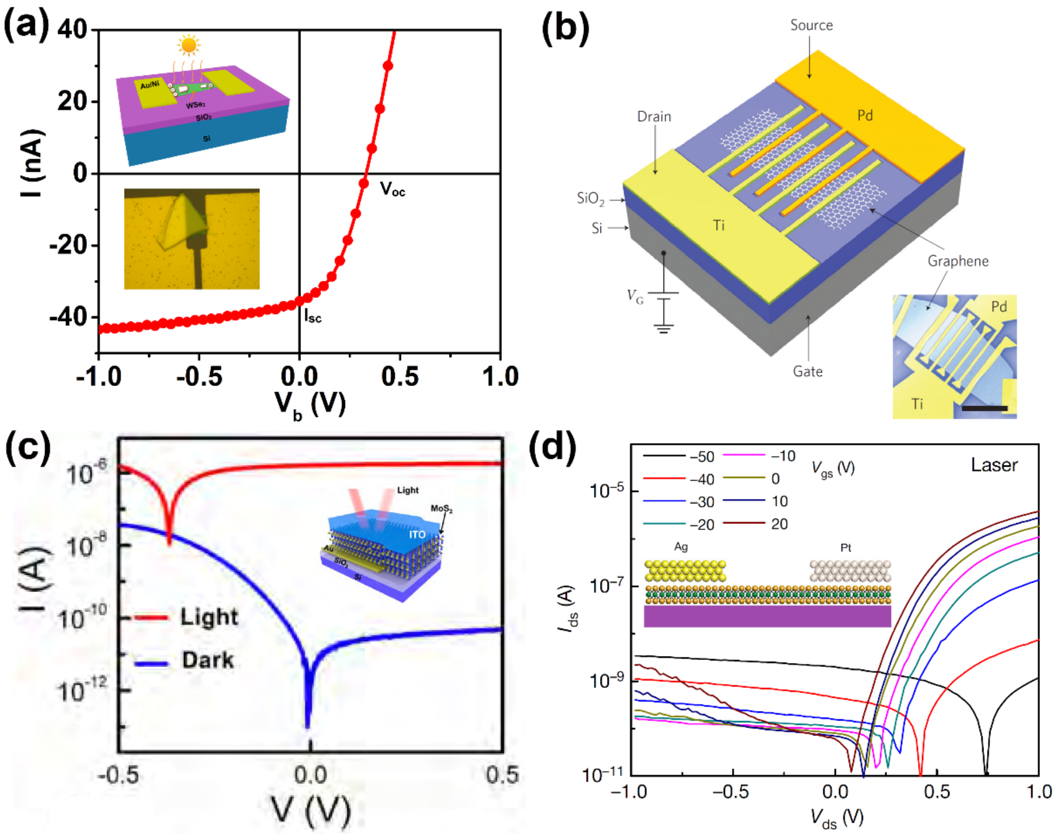

Figure 1 (a) *I-V* curve of the MSM photodetector with asymmetrical contact geometry. Insets show the schematic operational principle and an optical image of the fabricated device with a large difference in contact length[16]. (b) Schematic illustration of a graphene-based self-driven photodetector with different electrodes[22]. (c) Performance of a MoS_2 based vertical MSM photodetector with ITO as the top electrode and Au as the bottom electrode. The inset shows the device structure[20]. (d) *I-V* curves of an Ag-MoS_2-Pt photodetector with van der Waals asymmetrical contacts. The inset shows the device structure[28].

For the same MSM structure, in certain cases, the photo-thermoelectric effect can dominate the overall photoresponse, especially in the infrared range. The MS junction generates a photovoltage based on the temperature gradient induced by photon absorption. Thus, the MSM structure would require a local illumination strategy on one MS junction to generate a net non-zero I_{sc}, which is rarely realized in practical applications. Alternatively, if the two MS junctions exhibit different temperature gradients, a net I_{sc} can be expected. Recently, Safaei *et al.* designed a graphene-based MSM structure with asymmetrical contact[30]. For one side, the graphene is patterned and etched by oxygen plasma, leaving periodically nanoholes in the single-layer graphene to contact the Au electrode. For the opposite side, the graphene is smooth in contact with the Au electrode. Upon light illumination with 8-12 μm wavelength, the nanopatterned graphene-metal junction heats up more than the other side due to the plasmonic effect. As a result, a room-temperature infrared photodetector with a high responsivity of 2900 V/W is obtained in the 8-12 μm range, and a net I_{sc} is expected under light illumination due to the asymmetrical thermoelectric effect.

2.2 Field-induced asymmetry

For certain 2D materials exhibiting intrinsic piezoelectric, ferroelectric, pyroelectric or ferromagnetic effects[31], an external strain field or magnetic field can directly couple with the electric field and change the symmetry of the device structure. For example, single-layer MoS_2 exhibits intrinsic piezoelectric effect[32] and has been adopted to construct high-performance photovoltaic devices[33-35]. Zheng *et al.* theoretically investigated the strain-induced photovoltaic effect in a single-layer MoS_2 based metal-semiconductor Schottky junction[33]. Figure 2a schematically illustrates the operation principle of the device. When a tensile or compressive stress is applied between the two sides, respectively, corresponding piezoelectric polarization charges with opposite sign are induced at the two sides of MoS_2, which effectively changes the barrier height of the Schottky junction. According to their calculation, the V_{oc} can be increased by 5.8% at a strain of 1% [33]. Experimentally, Lin *et al.* prepared a van der Waals MoS_2/WSe_2 heterostructure on a flexible substrate and reported an enhanced responsivity of 86% when a compressive strain of 0.62% is induced along the armchair direction of MoS_2, suggesting that the piezoelectric charge induced energy band realignment is responsible for the performance improvement[34]. Figure 2b shows the measured dynamic photocurrent under a zero bias[34], in which the strain tunable photovoltaic is clearly demonstrated.

The bulk photovoltaic (BPV) effect is reported for some ferroelectric materials lacking a center of inversion symmetry. A shift current can be generated in these materials without forming a PN junction or Schottky junction. It is the internal polarization field that separates the photogenerated carriers and induces a net I_{sc}. Historically, the BPV effect is observed in bulk ferroelectric materials including $BiTaO_3$, $BiFeO_3$, and $LiNbO_3$ which possess a wide bandgap and can only absorb ultraviolet light[36-38]. Recently, there has been increasing interest in pursuing novel narrow bandgap semiconductor with the BPV effect. Theoretically, Rangel *et al.* predicted a large shift current (~ 100 $\mu A/V^2$) for the single-layer Ge and Sn based monochalcogenides including GeS, GeSe, SnS, and SnSe which also possess an energy bandgap corresponding to the visible light spectrum[39]. In addition, ferroelectric GeTe, magnet CrI_3, etc. have also been predicted to possess the BPV effect based on density functional theory calculations[40, 41]. Kushnir *et al.* proved the existence of shift current in the bulk GeS and GeSe by using terahertz emission spectroscopy[42, 43]. While this all-optical method only provides indirect proof of the BPV effect, most recently, Zhang *et al.* investigated the BPV effect of WS_2 devices with different crystal symmetry, including a single-layer WS_2, a bilayer WS_2, and a multi-walled WS_2 nanotube[44]. They observed an enhanced BPV effect for the WS_2 nanotube (Figure 2c), but there is no sign of BPV for the single-layer WS_2 which in principle is also a material without a center of inversion symmetry. This is probably due to the much smaller BPV induced I_{sc} than that induced at the Schottky contacts. Recently, it is proposed that the BPV effect can be also induced by exerting strain gradient in any semiconductor materials without the stringent requirement of non-centrosymmetric structure, which is denoted as flexo-photovoltaic (FPV) effect[45]. Strain gradients are introduced through either an atomic force microscope or a micrometer-scale indentation system. Large I_{sc} from centrosymmetric single crystals including $SrTiO_3$, TiO_2, and Si are obtained. Figure 2d shows the photocurrent versus voltage curves of the $SrTiO_3$ crystal under a 4 N force applied through a needle probe. The strain field induced photovoltaic effect can be extended to build 2D materials based self-driven photodetector.

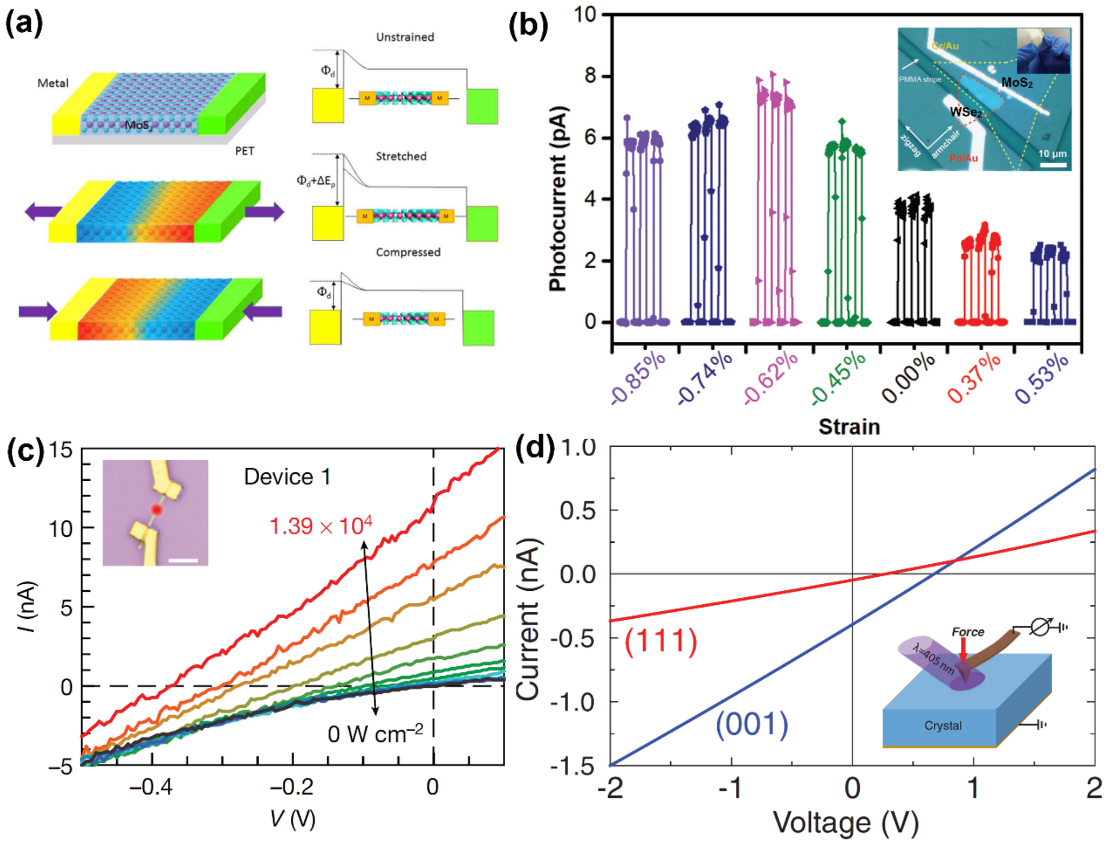

Figure 2 (a) Operation principle of the piezoelectric field induced barrier changes in a MoS2 based photodetector[33]. (b) Dependence of the short-circuit dynamic photocurrent on the applied strain. The inset shows the optical image of the device[34]. (c) I-V curves of the WS_2 nanotube showing the bulk photovoltaic effect. The inset shows the optical image of the device[44]. (d) Strain-induced bulk photovoltaic effect in $SrTiO_3$. The inset shows the measurement setup[45].

Pyroelectric materials have been widely adopted in infrared photodetectors. As most 2D materials cannot absorb infrared light, the pyroelectric effect provides an extra degree of freedom to design infrared photodetectors based on 2D materials. Kumar *et al.* reported an SnS based broadband self-driven photodetector that can detect near-infrared light (850 nm) through the pyroelectric effect[46]. However, the self-driven property originates from the SnS-Si junction, and the pyroelectric effect in SnS only helps to improve the responsivity. Although recent theoretical calculations predicted the existence of pyroelectric single-layer 2D materials[47], there is a lack of experimental evidence. Alternatively, integrating 2D material with pyroelectric bulk substrate provides a platform to utilize the pyroelectric field for infrared photodetectors. Sassi *et al.* demonstrated a graphene-based infrared detector by incorporating pyroelectric $LiNbO_3$ as the substrate and obtained an enhanced temperature coefficient of resistance up to 900% K^{-1}, as well as the ability to resolve temperature variations down to 15 μK [48].

2.3 PN homojunction

The mainstream silicon photodetector is based on the photovoltaic effect of the PN junction, in which the built-in field between a P-type and an N-type silicon separates the photogenerated carriers. In terms of 2D materials, the mature ion-implantation for doping silicon cannot be used as it will induce tremendous defects to the atomic structure of the 2D materials. Alternatively, various methods including stacking in situ doped materials[49-51], thickness engineering[52, 53], adopting a split gate[54-56], and novel doping strategies[57-61] have been proposed to realize the PN homojunction.

Jin *et al.* fabricated a vertical PN homojunction by physically overlapping a 3.2 nm-thick n-$MoSe_2$ on the transferred 2.9 nm-thick p-$MoSe_2$[49]. P-type $MoSe_2$ is formed by replacing Mo in $MoSe_2$ with Nb atoms. The fabricated PN junction reveals typical rectifying behavior at room temperature, and a V_{oc} of 0.35 V is obtained under light illumination (Figure 3a). Huo *et al.* reported an ultrasensitive photodetector implemented by an out-of-plane MoS_2 PN homojunction, and an ultrahigh specific detectivity of 3.5×10^{14} Jones is obtained in the visible spectrum [50]. A deep ultraviolet light-driven doping technique is developed to modulate the carrier concentration in a multilayer p-$MoTe_2$ flake, which is consequently inverted to n-$MoTe_2$, thus forming a van der Waals p-$MoTe_2$/n-$MoTe_2$ PN homojunction[51]. The ideality factor of 1.05 indicates a good interface quality, and clear photovoltaic characteristics have been observed.

Taking advantage of the thickness-dependent electronic and optoelectronic properties[62], PN homojunction can be constructed between two regions of the same material with different thicknesses[52, 53]. Yang *et al.* investigated a $MoSe_2$ homojunction formed between a 4 nm thick and a 28 nm thick flake (Inset of Figure 3b)[52]. The homojunction exhibits a V_{oc} of 0.24 V and a responsivity of ~ 1 A/W under zero bias. The photovoltaic effect shows the gate-tunable effect and is stable under varying gate voltage bias, as shown in Figure 3b. Kallatt *et al.* investigated the photoresponse to scanning photo-excitation in monolayer, bilayer, monolayer/bilayer, and monolayer/few-layer/multi-layer MoS_2 devices[53]. It is found that a thicker layer at the source is more effective in reducing the trap induced source barrier height reduction effect. When the laser is focused exactly at the monolayer/few-layer junction, the photo-generated electrons and holes are spatially separated. They are driven by the asymmetric potential barrier, so a strong photo-response is observed.

Asymmetry can be induced by the electric field in a homogenous material to form the PN homojunction[54-56]. Baugher *et al.* reported a monolayer WSe_2 PN junction enabled by split gates[55]. The schematic of the device is shown in the inset of Figure 3c. The voltages on the two gates (V_{gl} for the left gate and V_{gr} for the right gate) independently control the carrier density in the left and right sides of the monolayer, thereby electrostatically doping the device into various conductive modes. By oppositely biasing the two gates (V_{gl} = -40 V, V_{gr} = 40 V, denoted PN; V_{gl} = 40 V, V_{gr} = -40 V, denoted NP), the device rectifies current as a PN junction. In PN and NP configurations, the device exhibits a clear photovoltaic effect. A similar double gate structure has also been applied to other 2D materials such as a few-layer black-phosphorus for near-infrared light detection[54].

Selectively doping of a part of the 2D material to change the carrier polarity provides another way to form a PN homojunction. Both chemical and physical methods have been demonstrated successfully to effectively change the carrier concentration and carrier type. Yang *et al.* formed a WSe_2 PN junction by locally doping the originally P-type WSe_2[58]. During the chemical treatment, half of the WSe_2 flake is coated with Al_2O_3, while the remaining part is rinsed in diluted hydrazine hydrate for electron doping (Inset of Figure 3d). The lateral PN homojunction formed at the interface exhibits ideal diode behavior, and a large V_{oc} of ~ 0.8 V is obtained. Under a zero bias, a responsivity of 254 mA/W and a high on/off ratio of 10^3 are achieved (Figure 3d). Similarly, $AuCl_3$ was adopted to perform hole doping in pristine N-type MoS_2 for PN homojunction[57, 63]. Apart from the chemical doping strategy, physical doping by taking advantage of the dielectric interface is more stable and has been recently adopted in constructing a black-phosphorus PN homojunction[61].

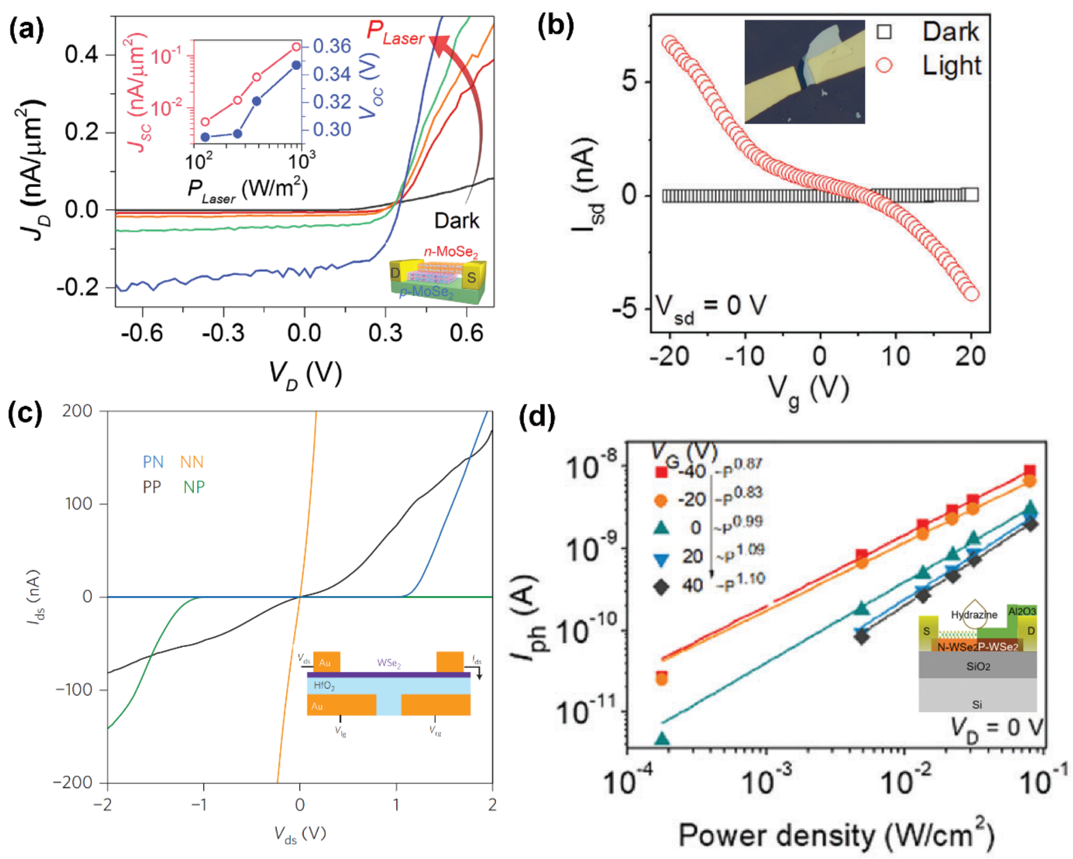

Figure 3 (a) *I-V* curves of the vertical $MoSe_2$ PN homojunction. Inset shows the device structure and dependence of J_{sc} and V_{oc} on light power density[49]. (b) I_{sc} of a $MoSe_2$ homojunction with asymmetrical thicknesses at the two sides versus the gate voltage bias under dark and light illumination. The inset shows the device optical image[52]. (c) *I-V* curves of the double-gate WSe_2 homojunction under different gate bias configurations. The inset shows the schematic side view of WSe_2 PN homojunction[55]. (d) Dependence of photocurrent on the light power density for a WSe_2 PN homojunction formed by locally chemical doping. Inset is a schematic view of the device structure[58].

2.4 PN heterojunctions formed by stacking method and direct synthesis

Van der Waals heterostructures, in which 2D materials are stacked on top of each other by transfer method[64], allow different materials with striking different lattice constants and physical properties to be combined for constructing novel devices, and PN heterojunction can be formed by choosing two materials with different carrier polarities[65-75]. Pezeshki *et al.* fabricated a van der Waals PN heterojunction by stacking P-type α-$MoTe_2$ onto N-type MoS_2[65]. To form Ohmic contacts, they chose Ti and Pt as the contacting electrodes for MoS_2 and $MoTe_2$, respectively, as shown in the inset of Figure 4a [65]. An ideality factor of ~1.06 is extracted for the PN heterojunction fabricated on a glass substrate. The photovoltaic effect is observed under light illuminations with various wavelengths, as shown in Figure 4a, and the highest responsivity of 322 mA/W under zero bias is recorded under blue light illumination. Tan *et al.* fabricated a PN heterojunction by vertically stacking a multilayer P-type GeSe on top of a thin N-type MoS_2 (1-3 layers) and studied its carrier transport and photoresponse properties[66]. The strong nonlinearity and asymmetry of the *I–V* curve proves the diode rectification function. However, the measured I_{sc} and V_{oc} are less than 5 pA and 50 mV, respectively, which is probably due to the same electrode material used for both P-type and N-type contacts.

Yang *et al.* demonstrated a P-type GaTe/N-type MoS_2 heterojunction formed by dry transfer method[68]. The self-driven photodetector exhibits a relatively high responsivity of 1.365 A/W under zero bias. Electron-hole pairs generated by light are readily separated by large built-in potential formed at the GaTe-MoS_2 interface. As a result, a short response time of <10 ms along with a high on/off ratio of ~340 is achieved. For infrared light detection, a narrow bandgap material should be adopted[70, 75]. Recently, Bullock *et al.* demonstrated a black-phosphorus/MoS_2 heterojunction for mid-wave infrared detection at room temperature[70]. Although the photodetector exhibits a pronounced I_{sc}, the V_{oc} is quite small, as can be seen from Figure 4b[70]. The gate-tunable heterojunction is enabled due to the controllable carrier concentration by electric field effect, as recently demonstrated by Cheng *et al.* [72]. An asymmetric van der Waals heterostructure consists of a graphene gate, h-BN gate dielectric, and vertically stacked MoS_2/$MoTe_2$ on top of h-BN (inset of Figure 4c), can function as a high-performance diode, transistor, photodetector, and programmable rectifier[72]. Figure 4c shows the *I–V* curves in the dark and in the presence of different intensity lasers, which shows an obvious photovoltaic effect.

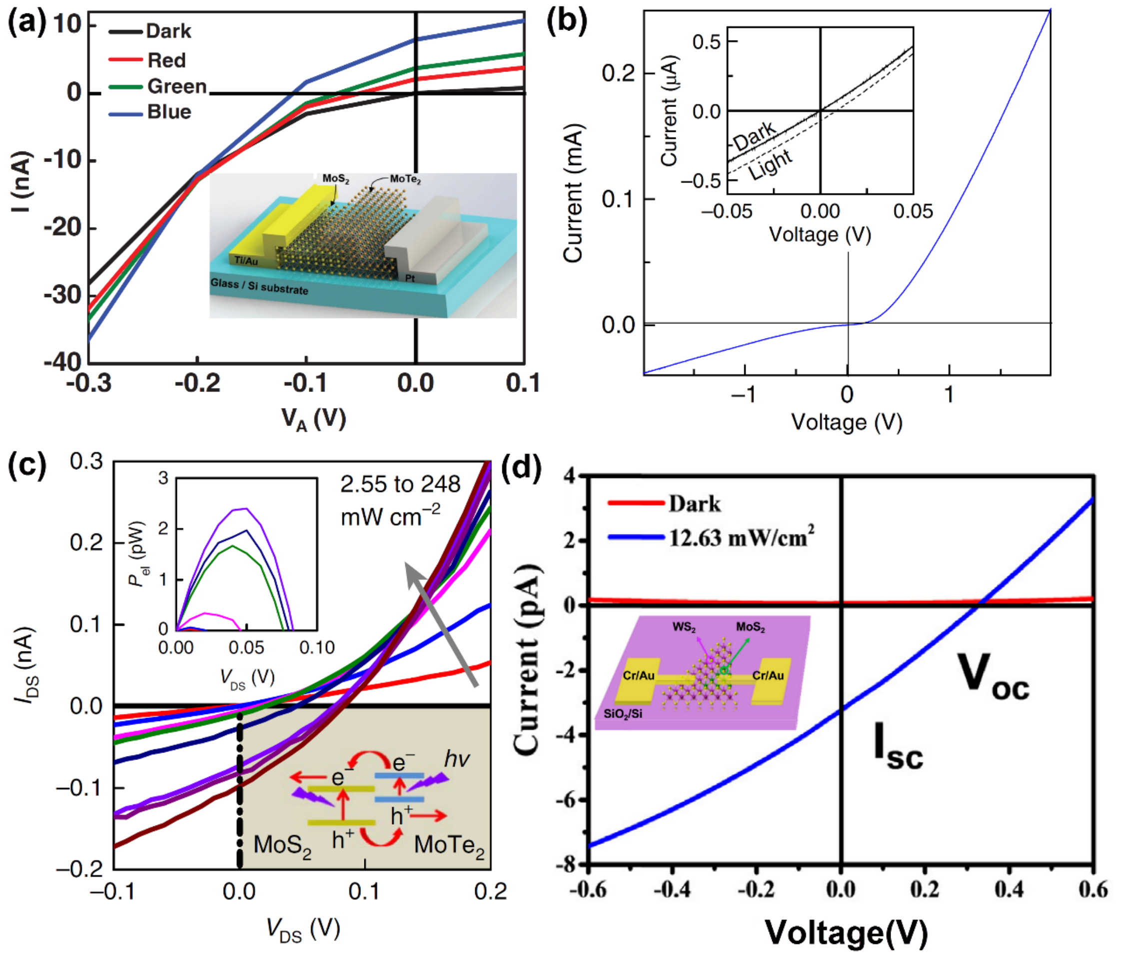

Figure 4 (a) *I–V* curves of $MoTe_2/MoS_2$ heterojunction under various laser wavelengths. Inset shows a schematic of the heterojunction[65]. (b) Self-driven behavior of black-phosphorus/MoS_2 heterostructure (V_{ds} = 0 V)[70]. (c) *I–V* curves of the $MoS_2/MoTe_2$ heterostructure in the dark and in the presence of a laser [72]. (d) *I-V* curves of the lateral WS_2-MoS_2 heterojunction under dark and light illumination. The inset shows the schematic heterostructure[76].

Lateral heterojunction refers to the connection of two 2D materials in the same plane, which usually forms a seamless interface at the junction[76-78]. The lateral heterojunction has the maximum built-in potential at the interface, which can quickly separate photogenerated electron-hole pairs without external bias, which makes it promising for self-driven photodetectors. Wu *et al.* prepared lateral MoS_2-WS_2 heterostructures with atomic thickness and sharp interface through a one-step synthesis strategy[76]. Single-layer MoS_2 flakes are laterally joint to the WS_2 parts (the inset of Figure 4d) and two different materials coexistence within a monolayer triangular domain, forming atomic sharp heterointerface due to their comparable lattice constants. Figure 4d presents the *I-V* curves near 0 V bias, demonstrating the obvious photovoltaic characteristic with a V_{oc} of 0.32 V and an I_{sc} of 3.5 pA under incident light of 12.63 mW/cm^2. Sahoo *et al.* reported a one-pot synthetic approach for the continuous fabrication of lateral multi-junction heterostructures consisting of monolayers of transition-metal dichalcogenides[78]. The sequential formation of heterojunctions is achieved solely by changing the composition of the reactive gas environment in the presence of water vapor.

3. Comparisons and Perspectives

Device fabrication complexity: For self-driven MSM photodetectors, an extra process step is required to form the asymmetrical contacts. That could be the patterning and etching process to form the asymmetrical contact geometry, or the extra metal electrode deposition and etching process for asymmetrical metal electrodes. On the other hand, the fabrication process is compatible with traditional CMOS technology, and the potential integration of the MSM structure with silicon circuits are readily obtained once the growth and transfer process of 2D materials becomes mature to be adopted for large-scale device development[79]. Comparatively, the field-induced asymmetry has stringent requirements on the material property itself, which is limited to certain functional materials. Alternatively, one can integrate the 2D material with a certain substrate with piezoelectric, ferroelectric effect, etc., in which case the field is induced by the underlying substrate. For the latter case, the photodetector cannot be integrated with the silicon substrate. In terms of the PN homojunction, its fabrication process is the same as a silicon photodiode, but the most difficult step is the controlled stable doping in 2D materials, which is still under development. Another key point that is usually overlooked in present studies is the Ohmic contacts required for both P-type and N-type 2D materials also involve different metal electrodes, which makes the fabrication process more complex than that of MSM photodetectors. Multiple transfer process and accurate positioning technology are needed for the construction of van der Waals heterostructures, which increase the fabrication complexity, and the van der Waals gap at the junction can hinder the charge transfer and degrade junction quality. Direct epitaxial growth using a chemical vapor deposition technique has been developed to grow heterojunctions. If the epitaxial method is further optimized to grow multilayer heterojunctions, high absorption and thus a high responsivity can be obtained, and it would provide a promising platform for large-scale self-driven photodetectors.

Performance evaluation: There are many parameters in determining the performance of a photodetector, including responsivity, response speed, photocurrent to dark current on/off ratio, linearity, and dynamic range. While some 2D materials based photodetectors exhibit ultrahigh responsivity or ultrafast response speed, there is a trade-off between the two parameters, which means a high responsivity is always accompanied by a slow response speed[80]. For self-driven characteristics, the photocurrent to dark current ratio is an important indicator for low-power applications. We note that although many 2D photodetectors report good responsivity and response speed, the linearity and dynamic range are rarely addressed[81, 82]. When considering a practical application such as imaging, the photodetectors are required to be integrated with data processing circuits, and the linearity and dynamic range directly relates to the complexity of the circuit design. In terms of responsivity, MSM photodetectors exhibit a reasonably high value of larger than 1 A/W, and PN junctions based on single to few-layer 2D materials exhibit lower values which are mainly due to the low absorption of the thin material. The photodetectors based on the BPV effect exhibit very low photocurrent in the pA to nA range[38, 45] and great challenges remain before adopting this effect for practical applications. It is noteworthy that for a silicon photodiode the responsivity is less than 1A/W, and the linearity is less than 5% within the dynamic range of 60 dB[6, 83]. Thus, the hurdle to practical application is not really the responsivity or response speed. We recommend that future performance evaluation should be more focused on the linearity and dynamic range, and on/off ratio especially for low-power applications.

4. Summary

With the rapid development of the semiconductor industry, low-power and self-driven devices become an indispensable part of the electronic components and optoelectronic products. 2D materials based self-driven photodetectors have been extensively studied for their excellent photoresponse and become an important part of self-driven photodetectors. In this review, by elaborating the concept of symmetry breaking in 2D materials based photodetector, we give a concise and generalized framework which covers existing photodetectors with self-driven properties. We provide a perspective to include the asymmetrical contact engineering, field-induced asymmetry, bulk photovoltaic, PN junction and van der Waals heterostructure into the same symmetry breaking framework, which is helpful for readers from different disciplines to understand the numerous reports on 2D materials based photodetectors. Self-driven photodetectors based on 2D materials have already exhibited good responsivity and fast response speed, and future research should be directed to focus on the linearity, dynamic range, and on/off ratio for practical low-power applications in IoT and wearable electronics.

Acknowledgement

This research was supported by the International Science & Technology Cooperation Program of Guangdong Province (2019A050510011), National Science Foundation of China (11804102), the Science and Technology Program of Guangzhou (201804010393, 201807010072), and the Research Grant Council of Hong Kong (15205619). Changjian Zhou would like to acknowledge the support from Guangdong Pearl River Youth Talent Recruitment Program.

1. Y. Kato, T. Sano, Y. Moriyama, S. Maeda, T. Yamazaki, A. Nose, K. Shiina, Y. Yasu, W. van der Tempel, A. Ercan, Y. Ebiko, D. Van Nieuwenhove and S. Sukegawa, *IEEE Journal of Solid-State Circuits*, 2018, **53**, 1071-1078.
2. G. H. Rieke, *Annual Review of Astronomy and Astrophysics*, 2007, **45**, 77-115.
3. J. S. Tyo, D. L. Goldstein, D. B. Chenault and J. A. Shaw, *Appl Opt*, 2006, **45**, 5453-5469.

4. C. W. Chow, R. J. Shiu, Y. C. Liu, Y. Liu and C. H. Yeh, *Opt Express*, 2018, **26**, 7079-7084.
5. V. Namasivayam, R. Lin, B. Johnson, S. Brahmasandra, Z. Razzacki, D. T. Burke and M. A. Burns, *Journal of Micromechanics and Microengineering*, 2004, **14**, 81-90.
6. M. Bigas, E. Cabruja, J. Forest and J. Salvi, *Microelectronics Journal*, 2006, **37**, 433-451.
7. G. Konstantatos and E. H. Sargent, *Nat Nanotechnol*, 2010, **5**, 391-400.
8. M. Buscema, J. O. Island, D. J. Groenendijk, S. I. Blanter, G. A. Steele, H. S. J. van der Zant and A. Castellanos-Gomez, *Chemical Society Reviews*, 2015, **44**, 3691-3718.
9. K. F. Mak and J. Shan, *Nature Photonics*, 2016, **10**, 216-226.
10. C. M. Nguyen, J. Mays, D. Plesa, S. Rao, M. Nguyen and J. C. Chiao, presented in part at the 2015 IEEE MTT-S International Microwave Symposium, 2015.
11. J. Liu, G. Faulkner, B. Choubey, S. Collins and D. C. O'Brien, *IEEE Sensors Journal*, 2018, **18**, 5321-5328.
12. S. Cai, X. Xu, W. Yang, J. Chen and X. Fang, *Adv Mater*, 2019, **31**, e1808138.
13. F. Xia, H. Wang, D. Xiao, M. Dubey and A. Ramasubramaniam, *Nature Photonics*, 2014, **8**, 899-907.
14. D. Akinwande, C. Huyghebaert, C. H. Wang, M. I. Serna, S. Goossens, L. J. Li, H. P. Wong and F. H. L. Koppens, *Nature*, 2019, **573**, 507-518.
15. Y. Xu, X. Chen, D. Zhou, F. Ren, J. Zhou, S. Bai, H. Lu, S. Gu, R. Zhang, Y. Zheng and J. Ye, *IEEE Transactions on Electron Devices*, 2019, **66**, 2276-2281.
16. C. Zhou, S. Raju, B. Li, M. Chan, Y. Chai and C. Y. Yang, *Advanced Functional Materials*, 2018, **28**, 1802954.
17. L. Ravikiran, K. Radhakrishnan, N. Dharmarasu, M. Agrawal, Z. Wang, A. Bruno, C. Soci, T. Lihuang and K. S. Ang, *IEEE Sensors Journal*, 2017, **17**, 72-77.
18. J. J. Chen, Q. Wang, J. Meng, X. Ke, G. Van Tendeloo, Y. Q. Bie, J. Liu, K. Liu, Z. M. Liao, D. Sun and D. Yu, *ACS Nano*, 2015, **9**, 8851-8858.
19. M. Dai, H. Chen, R. Feng, W. Feng, Y. Hu, H. Yang, G. Liu, X. Chen, J. Zhang, C. Y. Xu and P. Hu, *ACS Nano*, 2018, **12**, 8739-8747.
20. F. Gong, H. Fang, P. Wang, M. Su, Q. Li, J. C. Ho, X. Chen, W. Lu, L. Liao, J. Wang and W. Hu, *Nanotechnology*, 2017, **28**, 484002.
21. J. Liu, N. Guo, X. Xiao, K. Zhang, Y. Jia, S. Zhou, Y. Wu, Q. Li and L. Xiao, *Nanoscale Res Lett*, 2017, **12**, 603.
22. T. Mueller, F. Xia and P. Avouris, *Nature Photonics*, 2010, **4**, 297-301.
23. X. Wei, F. Yan, Q. Lv, W. Zhu, C. Hu, A. Patanè and K. Wang, *Advanced Optical Materials*, 2019, **7**, 1900190.
24. J. Yao, Z. Zheng, J. Shao and G. Yang, *ACS Appl Mater Interfaces*, 2015, **7**, 26701-26708.
25. W. J. Yu, Y. Liu, H. Zhou, A. Yin, Z. Li, Y. Huang and X. Duan, *Nat Nanotechnol*, 2013, **8**, 952-958.
26. K. Zhang, X. Fang, Y. Wang, Y. Wan, Q. Song, W. Zhai, Y. Li, G. Ran, Y. Ye and L. Dai, *ACS Appl Mater Interfaces*, 2017, **9**, 5392-5398.

27. M. Fontana, T. Deppe, A. K. Boyd, M. Rinzan, A. Y. Liu, M. Paranjape and P. Barbara, *Sci Rep*, 2013, **3**, 1634.
28. Y. Liu, J. Guo, E. Zhu, L. Liao, S.-J. Lee, M. Ding, I. Shakir, V. Gambin, Y. Huang and X. Duan, *Nature*, 2018, **557**, 696-700.
29. J. Wang, X. Guo, Z. Yu, Z. Ma, Y. Liu, M. Chan, Y. Zhu, X. Wang and Y. Chai, presented in part at the 2018 IEEE International Electron Devices Meeting (IEDM), 2018.
30. A. Safaei, S. Chandra, M. W. Shabbir, M. N. Leuenberger and D. Chanda, *Nature Communications*, 2019, **10**, 3498.
31. C. Cui, F. Xue, W.-J. Hu and L.-J. Li, *npj 2D Materials and Applications*, 2018, **2**, 18.
32. W. Wu, L. Wang, Y. Li, F. Zhang, L. Lin, S. Niu, D. Chenet, X. Zhang, Y. Hao, T. F. Heinz, J. Hone and Z. L. Wang, *Nature*, 2014, **514**, 470-474.
33. D. Q. Zheng, Z. Zhao, R. Huang, J. Nie, L. Li and Y. Zhang, *Nano Energy*, 2017, **32**, 448-453.
34. P. Lin, L. Zhu, D. Li, L. Xu, C. Pan and Z. Wang, *Advanced Functional Materials*, 2018, **28**, 1802849.
35. X. Liu, X. Yang, G. Gao, Z. Yang, H. Liu, Q. Li, Z. Lou, G. Shen, L. Liao, C. Pan and Z. Lin Wang, *ACS Nano*, 2016, **10**, 7451-7457.
36. J. E. Spanier, V. M. Fridkin, A. M. Rappe, A. R. Akbashev, A. Polemi, Y. Qi, Z. Gu, S. M. Young, C. J. Hawley, D. Imbrenda, G. Xiao, A. L. Bennett-Jackson and C. L. Johnson, *Nature Photonics*, 2016, **10**, 611-616.
37. A. Bhatnagar, A. Roy Chaudhuri, Y. Heon Kim, D. Hesse and M. Alexe, *Nature Communications*, 2013, **4**, 2835.
38. S. Nadupalli, J. Kreisel and T. Granzow, *Sci Adv*, 2019, **5**, eaau9199.
39. T. Rangel, B. M. Fregoso, B. S. Mendoza, T. Morimoto, J. E. Moore and J. B. Neaton, *Phys Rev Lett*, 2017, **119**, 067402.
40. S. J. Gong, F. Zheng and A. M. Rappe, *Phys Rev Lett*, 2018, **121**, 017402.
41. Y. Zhang, T. Holder, H. Ishizuka, F. de Juan, N. Nagaosa, C. Felser and B. Yan, *Nat Commun*, 2019, **10**, 3783.
42. K. Kushnir, M. Wang, P. D. Fitzgerald, K. J. Koski and L. V. Titova, *ACS Energy Letters*, 2017, **2**, 1429-1434.
43. K. Kushnir, Y. Qin, Y. Shen, G. Li, B. M. Fregoso, S. Tongay and L. V. Titova, *ACS Appl Mater Interfaces*, 2019, **11**, 5492-5498.
44. Y. J. Zhang, T. Ideue, M. Onga, F. Qin, R. Suzuki, A. Zak, R. Tenne, J. H. Smet and Y. Iwasa, *Nature*, 2019, **570**, 349-353.
45. M. M. Yang, D. J. Kim and M. Alexe, *Science*, 2018, **360**, 904-907.
46. M. Kumar, M. Patel, J. Kim and D. Lim, *Nanoscale*, 2017, **9**, 19201-19208.
47. J. Liu and S. T. Pantelides, *Phys Rev Lett*, 2018, **120**, 207602.
48. U. Sassi, R. Parret, S. Nanot, M. Bruna, S. Borini, D. De Fazio, Z. Zhao, E. Lidorikis, F. H. Koppens, A. C. Ferrari and A. Colli, *Nat Commun*, 2017, **8**, 14311.
49. Y. Jin, D. H. Keum, S. J. An, J. Kim, H. S. Lee and Y. H. Lee, *Adv Mater*, 2015, **27**, 5534-5540.

50. N. Huo and G. Konstantatos, *Nat Commun*, 2017, **8**, 572.
51. S. Aftab, M. F. Khan, P. Gautam, H. Noh and J. Eom, *Nanoscale*, 2019, **11**, 9518-9525.
52. Y. Yang, N. Huo and J. Li, *Journal of Materials Chemistry C*, 2017, **5**, 7051-7056.
53. S. Kallatt, G. Umesh, N. Bhat and K. Majumdar, *Nanoscale*, 2016, **8**, 15213-15222.
54. M. Buscema, D. J. Groenendijk, G. A. Steele, H. S. van der Zant and A. Castellanos-Gomez, *Nat Commun*, 2014, **5**, 4651.
55. B. W. Baugher, H. O. Churchill, Y. Yang and P. Jarillo-Herrero, *Nat Nanotechnol*, 2014, **9**, 262-267.
56. J. S. Ross, P. Klement, A. M. Jones, N. J. Ghimire, J. Yan, D. G. Mandrus, T. Taniguchi, K. Watanabe, K. Kitamura, W. Yao, D. H. Cobden and X. Xu, *Nat Nanotechnol*, 2014, **9**, 268-272.
57. H. M. Li, D. Lee, D. Qu, X. Liu, J. Ryu, A. Seabaugh and W. J. Yoo, *Nat Commun*, 2015, **6**, 6564.
58. Y. Yang, N. Huo and J. Li, *Journal of Materials Chemistry C*, 2018, **6**, 11673-11678.
59. J. Sun, Y. Wang, S. Guo, B. Wan, L. Dong, Y. Gu, C. Song, C. Pan, Q. Zhang, L. Gu, F. Pan and J. Zhang, *Adv Mater*, 2020, DOI: 10.1002/adma.201906499, e1906499.
60. M. Sun, D. Xie, Y. Sun, W. Li and T. Ren, *Nanotechnology*, 2018, **29**, 015203.
61. Y. Xu, C. Liu, C. Guo, Q. Yu, W. Guo, W. Lu, X. Chen, L. Wang and K. Zhang, *Nano Energy*, 2020, **70**, 104518.
62. C. Zhou, Y. Zhao, S. Raju, Y. Wang, Z. Lin, M. Chan and Y. Chai, *Advanced Functional Materials*, 2016, **26**, 4223-4230.
63. M. S. Choi, D. Qu, D. Lee, X. Liu, K. Watanabe, T. Taniguchi and W. J. Yoo, *ACS Nano*, 2014, **8**, 9332-9340.
64. A. Castellanos-Gomez, M. Buscema, R. Molenaar, V. Singh, L. Janssen, H. S. J. van der Zant and G. A. Steele, *2D Materials*, 2014, **1**, 011002.
65. A. Pezeshki, S. H. Shokouh, T. Nazari, K. Oh and S. Im, *Adv Mater*, 2016, **28**, 3216-3222.
66. D. Tan, X. Wang, W. Zhang, H. E. Lim, K. Shinokita, Y. Miyauchi, M. Maruyama, S. Okada and K. Matsuda, *Small*, 2018, **14**, e1704559.
67. J. Shim, S. W. Jang, J. H. Lim, H. Kim, D. H. Kang, K. H. Kim, S. Seo, K. Heo, C. Shin, H. Y. Yu, S. Lee, D. H. Ko and J. H. Park, *Nanoscale*, 2019, **11**, 12871-12877.
68. S. Yang, C. Wang, C. Ataca, Y. Li, H. Chen, H. Cai, A. Suslu, J. C. Grossman, C. Jiang, Q. Liu and S. Tongay, *ACS Appl Mater Interfaces*, 2016, **8**, 2533-2539.
69. M. H. Doan, Y. Jin, S. Adhikari, S. Lee, J. Zhao, S. C. Lim and Y. H. Lee, *ACS Nano*, 2017, **11**, 3832-3840.
70. J. Bullock, M. Amani, J. Cho, Y.-Z. Chen, G. H. Ahn, V. Adinolfi, V. R. Shrestha, Y. Gao, K. B. Crozier, Y.-L. Chueh and A. Javey, *Nature Photonics*,

2018, **12**, 601-607.
71. D. Li, B. Wang, M. Chen, J. Zhou and Z. Zhang, *Small*, 2017, **13**, 1603726.
72. R. Cheng, F. Wang, L. Yin, Z. Wang, Y. Wen, T. A. Shifa and J. He, *Nature Electronics*, 2018, **1**, 356-361.
73. F. Wang, L. Yin, Z. X. Wang, K. Xu, F. M. Wang, T. A. Shifa, Y. Huang, C. Jiang and J. He, *Advanced Functional Materials*, 2016, **26**, 5499-5506.
74. P. Wang, S. Liu, W. Luo, H. Fang, F. Gong, N. Guo, Z. G. Chen, J. Zou, Y. Huang, X. Zhou, J. Wang, X. Chen, W. Lu, F. Xiu and W. Hu, *Adv Mater*, 2017, **29**, 1604439.
75. R. Zhou, V. Ostwal and J. Appenzeller, *Nano Lett*, 2017, **17**, 4787-4792.
76. W. Wu, Q. Zhang, X. Zhou, L. Li, J. Su, F. Wang and T. Zhai, *Nano Energy*, 2018, **51**, 45-53.
77. C. Huang, S. Wu, A. M. Sanchez, J. J. Peters, R. Beanland, J. S. Ross, P. Rivera, W. Yao, D. H. Cobden and X. Xu, *Nat Mater*, 2014, **13**, 1096-1101.
78. P. K. Sahoo, S. Memaran, Y. Xin, L. Balicas and H. R. Gutierrez, *Nature*, 2018, **553**, 63-67.
79. N. Flory, P. Ma, Y. Salamin, A. Emboras, T. Taniguchi, K. Watanabe, J. Leuthold and L. Novotny, *Nat Nanotechnol*, 2020, **15**, 118-124.
80. G. Konstantatos, *Nat Commun*, 2018, **9**, 5266.
81. M. Buscema, J. O. Island, D. J. Groenendijk, S. I. Blanter, G. A. Steele, H. S. van der Zant and A. Castellanos-Gomez, *Chem Soc Rev*, 2015, **44**, 3691-3718.
82. C. Xie, C. Mak, X. Tao and F. Yan, *Advanced Functional Materials*, 2017, **27**, 1603886.
83. A. El Gamal and H. Eltoukhy, *IEEE Circuits and Devices Magazine*, 2005, **21**, 6-20.